A novel non-intrusive method to resolve the thermal-dome-effect of pyranometers: Radiometric calibration and implications

Q. Ji [1, 2], S.-C. Tsay [2], K. M. Lau [2], R. A. Hansell [1, 2], J. J. Butler [2], J. W. Cooper [3, 2]

[1] ESSIC/University of Maryland – College Park, College Park, Maryland, USA.

[2] Earth Sciences Division, NASA/GSFC, Greenbelt, Maryland, USA.

[3] Sigma Space Corp., Greenbelt, Maryland, USA.

Revised for submission to

Journal of Geophysical Research - Atmospheres

2011JD016466

30 September 2011

Corresponding author's address:

Dr. Q. Ji, c/o Code 613, NASA/Goddard Space Flight Center, MD 20771.

Tel: 301-614-6231, E-mail: qiang.ji-1@nasa.gov.

Abstract

Traditionally the calibration equation for pyranometers assumes that the measured solar irradiance is solely proportional to the thermopile's output voltage; therefore only a single calibration factor is derived. This causes additional measurement uncertainties because it does not capture sufficient information to correctly account for a pyranometer's thermal effect. In our updated calibration equation, temperatures from the pyranometer's dome and case are incorporated to describe the instrument's thermal behavior, and a new set of calibration constants are determined, thereby reducing measurement uncertainties.

In this paper, we demonstrate why a pyranometer's uncertainty using the traditional calibration equation is always larger than a-few-percent, but with the new approach can become much less than 1% after the thermal issue is resolved. The highlighted calibration results are based on NIST-traceable light sources under controlled laboratory conditions. The significance of the new approach lends itself to not only avoiding the uncertainty caused by a pyranometer's thermal effect but also the opportunity to better isolate and characterize other instrumental artifacts, such as angular response and non-linearity of the thermopile, to further reduce additional uncertainties. We also discuss some of the implications, including an example of how the thermal issue can potentially impact climate studies by evaluating aerosol's direct-radiative-effect using field measurements with and without considering the pyranometer's thermal effect. The results of radiative transfer model simulation show that a pyranometer's thermal effect on solar irradiance measurements at the surface can be translated into a significant alteration of the calculated distribution of solar energy inside the column atmosphere.

48 **1. Introduction**

49 The measurements of solar irradiance over the globe play an important role in climate
50 studies because solar radiation is the primary driving force of climate. Pyranometers are used
51 worldwide to measure solar irradiance. Traditionally, the uncertainty of a high quality
52 pyranometer is greater than a few percent, which is not desired for studying long-term climate
53 change. For example, the radiative forcing due to doubling the amount of CO_2 in the atmosphere
54 is ~4 W m^{-2} [*NAS* report, 1979], and the global average of radiative forcing for different agents
55 and mechanisms is around a couple of W m^{-2} [*IPCC* report, 2007]. However, a ±2% uncertainty
56 [e.g., *WMO* specification of pyranometer, 2008] on the ~184 W m^{-2} (~263 W m^{-2} if cloud-free)
57 global annual mean solar radiation at the Earth's surface [*Trenberth et al.*, 2009] is over ±3.6 W
58 m^{-2}, comparable to or larger than the expected ranges of the climate change signals. A reduced
59 uncertainty in pyranometer measurements will have profound implications, such as gaining the
60 ability to better discern the radiative forcing, or the global dimming and brightening [*Wild*,
61 2009]. Furthermore, a more accurate dataset of solar irradiance will also help improve the
62 evaluation of the effects of clouds and aerosols on climate studies. An example of the latter
63 effect is explored later in the paper.

64 A pyranometer's larger than 2~3% uncertainty [*WMO*, 2008] is related to its thermal-
65 dome-effect (TDE), which traditionally is not quantified. Shading a pyranometer can help reveal
66 and infer its thermal effect [e.g., *Gulbrandsen*, 1978]; however, it does not provide a direct non-
67 intrusive measurement of TDE. In addition, any object casting the shade also imposes its own
68 contribution dynamically to the thermal environment. This situation has changed since the
69 studies that explicitly describe the TDE [e.g., *Bush et al.*, 2000; *Ji and Tsay*, 2000; *Haeffeliin et*
70 *al.*, 2001; *Dutton et al.*, 2001]. Continuing the effort to directly addressing the thermal issue, *Ji*

and Tsay [2010] have introduced an innovative non-intrusive method that enables a reliable and routine monitoring of TDE; thus this thermal effect of pyranometer can be correctly accounted for in measurements of solar irradiance.

Historically, the measured solar irradiance, I, is regarded as being simply proportional to the output voltage of the pyranometer's thermopile, V:

$$I = c_h V, \tag{1}$$

where c_h is an empirical calibration factor. Regardless of how c_h is determined, this traditional calibration equation carries a large uncertainty because it is incapable of fully capturing the dynamic thermal behavior of the pyranometer. To reduce the uncertainty, we have derived a new calibration equation:

$$I = c V + f\sigma (T_s^4 - T_d^4), \tag{2}$$

where T_s is the temperature of the receiving surface of the thermopile, and T_d is the effective dome temperature. In addition, σ=5.67×10^{-8} J s^{-1} m^{-2} K^{-4} is the Stefan–Boltzmann constant; and the intrinsic calibration constants c and f are stable physical properties [*Ji and Tsay*, 2000]. f is also called the "dome factor", a quantity related to the dome emissivity and the geometry of a pyranometer (discussed in this paper). Furthermore, because the thermopile's output is referenced to the temperature of the pyranometer's case (i.e., T_c), T_s can be determined by $T_s = T_c + \alpha V$, where α is a thermopile parameter, and we regarded it as a constant in our previous study [*Ji and Tsay*, 2010]. A schematic of a pyranometer illustrating a couple of our non-intrusive methods for deriving T_d is described in Appendix A.

91 The difference between the traditional and the new calibration equations is obvious. The
92 former has one measurement (i.e., V) and a single empirical factor (i.e., c_h), unable to properly
93 represent the TDE; while the latter incorporates three measurements (i.e., V, T_c, and T_d) and four
94 true physical constants (i.e., c, f, σ, and α), able to quantify the TDE by the temperature-related
95 term. A variety of methods for calibrating pyranometers are listed in WMO's Guide to
96 Meteorological Instruments and Methods of Observations [*WMO*, Chapter 7.3.1, 2008]. Since
97 they all depend on Equation (1), we refer this type of calibration as a V1C1 calibration; standing
98 for one measured variable, and one constant to be determined. For example, whenever a single
99 calibration-constant is provided by a manufacture or a research laboratory such as Broadband
100 Outdoor Radiometer Calibrations [BORCAL at the National Renewable Energy Laboratory,
101 http://www.nrel.gov/aim/borcal.html], it is a V1C1 calibration. Under this convention a method
102 using Equation (2) becomes a V3C4 calibration. However, because σ is an universal constant,
103 and following our previous studies we assume α is a know constant, we are effectively dealing
104 with a V3C2 calibration in this study. Additionally, our new method is backward compatible,
105 because the V1C1 calibration remains intact and available.

106 A characteristic listed in the specification of a pyranometer [*WMO*, 2008] is its "zero
107 offset", but how it affects the uncertainty of a pyranometer is not specified. In order to correct the
108 offset errors in measurements of diffuse solar irradiance, *Dutton et al.* [2001] developed a data
109 correction procedure where the correction factor is derived from the output of a collocated
110 pyrgeometer that measures atmospheric infrared irradiance. This is an indirect approach
111 involving multiple instruments. These results are useful if the diffuse component is required
112 when calibrating total irradiance radiometers by reference to a standard pyrheliometer and a
113 shaded reference pyranometer [*ISO*, 1993]. The method is expensive if used in the routine

114 measurement of total irradiance because it requires a pyrheliometer for the direct solar
115 component, a shaded pyranometer for the diffuse sky component, and a shaded pyrgeometer for
116 the thermal correction of the shaded pyranometer. In addition, all three instruments must be
117 mounted on a solar tracker; and the pyranometer and pyrgeometer need to be ventilated. Another
118 complication is related to the pyrheliometer being subject to thermal effects (discussed in this
119 paper). In contrast, our new method eliminates the "zero offset" directly from a pyranometer [*Ji*
120 *and Tsay*, 2010].

121 Different design and make of pyranometers are available commercially. Their response to
122 thermal effect are different too [e.g., *Michalsky et al.*, 2003]. We focused on Epply PSP
123 [Precision Spectral Pyranometer, http://www.eppleylab.com], because its design has remained
124 relatively unchanged for decades; therefore, there are relatively longer records of consistent
125 measurement, which is useful for climate-change studies. Nevertheless, our new method and
126 discussions are not limited to PSP, we expect them to be also valuable in improving other
127 instruments and measurements.

128 This paper is structured as follows. In Section 2 we present our method for radiometric
129 calibration of a pyranometer against a calibrated NIST-traceable light source. In Section 3 we
130 show the measurement results illustrating the weakness of the V1C1 calibration and the
131 advantage of the V3C2 one. In Section 4 we discuss implications of this new approach, including
132 some of the knowledge gained, followed by an example of model simulation demonstrating the
133 potential impact of TDE on climate studies. Finally, the conclusion and future work are
134 presented in Section 5.

135

2. Radiometric calibration

In this study, integrating spheres maintained in a clean room of the Radiometric Calibration Facility at NASA Goddard Space Flight Center [http://spectral.gsfc.nasa.gov] are used as references to examine both the traditional and new calibration equations. Figure 1a illustrates a PSP mounted in front of an integrating sphere. This light source is calibrated by comparison with NIST-calibrated standard irradiance lamps using monochromators [*Walker et al.*, 1991]. Its spectral radiance is shown in Figure 1b.

The calibration procedure is straightforward: for V1C1, a calibration factor is determined by $c_h=\{I/V\}$ for Equation (1); for V3C2, c and f can be derived as the intercept and slope of a linear fit from $\{I/V\}=c+f\{\sigma(T_s^4-T_d^4)/V\}$ for Equation (2). In addition, although T_d is not directly measured, it can be verified under special conditions from T_c by maintaining a pyranometer in the dark until a thermal equilibrium state is achieved (i.e., $V=0$ and $T_d=T_c$).

Note that the parameter space over which the overall-calibration-uncertainty of a pyranometer can be adequately quantified is a much bigger question to tackle. To properly address this question will require the collective efforts of the scientific community as a whole whereby the current methodology can be fully tested in different environments under different situations. Here we regard a light source as an absolute radiometric reference for showing how V1C1 and V3C2 track a reference, thereby demonstrating why measurements can be improved.

3. Results

Eight rounds of calibration are depicted in Figure 2 as an example to illustrate the effects of TDE. The measured temperatures are shown in Figure 2a, where T_s and T_c are plotted as the thin curves at the top and on the bottom, respectively. In the middle is T_d shown as the bold curve, which is proportional to the pressure of the air sealed between the domes as plotted in Figure 2b.

This example reveals that T_s responds immediately when a PSP is exposed to light, while T_d changes slowly and T_c lags further behind. Naturally, in response to the "solar heating", the larger the thermal mass is, the smaller the rate of change will be. When it is blocked from light, T_s approaches T_c promptly while all the temperatures decrease, and the thermal gradient diminishes after several minutes. Once exposed to light the second time, all temperatures start to rise again, but begin with a higher value due to the heating in the previous round, and will reach higher levels. Notice that if we just reduce the intensity of light instead of fully blocking it to return the PSP to dark conditions, then T_d will decrease, but other temperatures may still be increasing with smaller rates under the reduced heating than in the previous round; however, all temperatures start to decrease if the irradiance is further reduced to a point that the heating became insufficient. In this example the irradiance was set to 879.6 W m^{-2} in rounds 1 and 2, then reduced to 668.3 W m^{-2} in rounds 3 to 5, and further reduced to 455.2 W m^{-2} in rounds 6 and 7, and finally to 244.3 W m^{-2} in round 8. Generally the system warms up in the early rounds when irradiance is larger and cools down later when irradiance becomes smaller, which to a certain extent represents morning and afternoon conditions, respectively.

It is important to point out that in each round of calibration the output voltage of the thermopile varies noticeably and does not reach a stable value for a prolonged period of time while the variation of the light source is negligible (less than 0.1%), as illustrated in Figure 2c.

179 The changing output voltage is cause by the TDE. In this example the transitional period lasted
180 about ten minutes in the first round when the temperature swing was relatively large. The
181 thermal gradient inside the PSP diminishes faster in the later rounds when the irradiance is
182 smaller.

183

184 **3.1. V1C1 calibration**

185 The limitation of a V1C1 calibration is demonstrated in Figure 3, where the curve shows
186 the calibration factor (i.e., I/V, or c_h). Evidently, c_h neither starts at a fixed value nor reaches a
187 fixed one in each round of calibration. This is unwanted for Equation (1), because it may make a
188 PSP's thermopile seemingly nonlinear against temperature. However, it is expected according to
189 Equation (2), which predicts that if I remains stable, then the larger the TDE, the smaller the V,
190 and vice versa.

191 Also marked in Figure 3 is a V1C1 calibration from BORCAL (i.e., c_h=133.95 W m^{-2}
192 mV^{-1}, +2.84%, -4.43%, for PSP#33109F3). Notice its large uncertainty range, which is typical
193 in a V1C1 method related to the lack of an accurate interpretation of the thermal effect. To
194 correct the errors in the V1C1 calibrated measurements, a correction method such as the one
195 developed by *Dutton et al.* [2001] is needed.

196

197 **3.2. V3C2 calibration**

198 The potential of using the V3C2 calibration equation is demonstrated in Figure 4a, where
199 the calibration constants (i.e., mean value ± standard deviation) are based on four rounds of

200 calibration; two each at I=879.6 and 668.3 W m^{-2}. Notice that the linearity of the curve is an
201 indication on how well Equation (2) can capture the reality. To show repeatability, Figure 4b
202 overlays twelve more rounds that include I=455.2, 244.3, also 960.3, 729.7, 497.0, and 266.7 W
203 m^{-2}; realized by turning on different lamps in the integrating sphere, and by altering the distance
204 between the PSP and the integrating sphere. In this particular example, the I/V versus $\sigma(T_s^4$-
205 $T_d^4)/V$ curve shifted slightly during those extra rounds when irradiances were smaller; however,
206 the slope (i.e., f) remains relatively unchanged after a shift, which is consistent with f being a
207 stable factor independent of the uncertainty in I and c. We found that the shift does not diminish
208 when the PSP's "thermopile temperature compensation circuit" is disabled, indicating that it is
209 not caused by the slight drift of temperature during these particular rounds. The shift can be
210 caused by several reasons, such as biases in I, nonlinearity in V, or error in T_d. Future work is
211 necessary to resolve the issue to further reduce the uncertainty.

212 In order to determine T_d, we sealed the space between the inner and outer domes of a PSP
213 to create a constant volume gas thermometer [*Ji and Tsay*, 2010]. This method is non-intrusive
214 because it does not block the field of view of thermopile; however, it modifies a PSP slightly. To
215 evaluate whether this modification impacts the performance of the PSP, we tested one of our
216 alternative methods that does not require such modification (see Appendix A). Although this
217 alternative method is less straightforward in determining T_d, and produces slightly more noise in
218 the calibration results as shown in Figure 4c, it indicates that a PSP's performance remains
219 consistent regardless of modification.

220

221 **3.3. Contrast between the two results**

An example of comparing the V1C1 and the V3C2 calibrations is given in Figure 5. When exposed to a known irradiance of 893.7 W m^{-2}, the V1C1 result reached 870 W m^{-2} initially, then drifted to 901 W m^{-2} in about ten minutes. Once repeated in the next round, it approached a couple of W m^{-2} lower, corresponding to about 1°C rise in temperature. In contrast, the result from the V3C2 calibration started to track the known irradiance within a few seconds every time. Figure 5b highlights a situation when light was blocked. After an initial drop, it took over ten minutes for the V1C1 calibrated result to decrease from about 30 to 0 W m^{-2}, while the V3C2 calibrated result promptly jumped to 0 W m^{-2}. The high precision of the new calibration is evident.

According to the WMO specification, the response time of a high quality pyranometer is less than 15 seconds. This is based on using a V1C1 calibration for the measurement to reach 95% of final value. In contrast, it will reach 99.9% of final value within 15 seconds in a V3C2 calibration. More importantly, the results from Equation (2) will remain consistent when the calibration is repeated, which reflects that because c and f represent stable physical properties their values can be more accurately determined over time with better statistics. This is unachievable in a V1C1 calibration, because the empirical factor in Equation (1) depends on environmental conditions and does not converge to a constant.

4. Implications

There are many important implications in realizing that a pyranometer can have a much smaller uncertainty once its thermal effect is accounted for. For example, we used to assign each PSP to a specific ventilator hoping the set would maintain a consistent thermal characteristic. We

244 also tried to use reversed ventilation to reduce the thermal effect. With the new calibration,
245 ventilation is rendered noncritical concerning the thermal effect. This makes it easy for us to
246 deploy a solar-powered network of PSPs and to generate a more consistent dataset, in light of
247 that a consistent global dataset is of importance for climate studies. A few other things we have
248 learned are briefly highlighted in the following.

249

250 **4.1. Different domes and dome factors**

251 We tested several "clear-domes" [WG295 glass, http://schottglass.com] on the same PSP,
252 and found that they yield a consistent result using the new calibration. Other than WG295, we
253 also use "color-domes", such as GG395, for selecting spectral bands from 0.4 to 3 μm and
254 RG695 for 0.7 to 3 μm. Traditionally a PSP is calibrated with a clear-dome; and when a color-
255 dome is needed for quantifying the energy partitioning in solar irradiance, an empirical scale
256 factor is applied. It is difficult to determine and to justify a scale factor without knowing the
257 TDE.

258 With Equation (2), we treat all types of domes equally except when considering the
259 corresponding spectral transmittance in the determination of the irradiance from the light source.
260 We found that an RG695's TDE changes faster and varies over a larger range, but can balance at
261 a smaller value than a WG295's. It is because an RG695 dome absorbs more solar radiation than
262 a WG295 dome does; therefore, its T_d becomes closer to T_s than with a WG295 dome. The
263 resulting distinct thermal behavior indicates that a scale factor is not appropriate for an RG695 in
264 terms of a highly accurate and consistent measurement.

As listed in Table 1, an RG695 dome has a slightly larger dome factor than a WG295 dome, which in turn has a slightly larger dome factor than a quartz dome (i.e., 1.8 vs. 1.5 vs. 1.3 for PSP#33109F3). In theory, for an idealized pyranometer whose thermopile's receiving surface occupies the whole area underneath the dome, its dome factor is the emissivity of dome which is smaller than 1.0 [*Ji and Tsay*, 2000]. In reality, the receiving surface in a PSP only covers a small fraction of the area, allowing its surroundings to contribute noticeably to TDE, leading to a larger "effective value" of f. It may be improved in the future with a better calibration equation.

4.2. Essence of thermal effect

To truly understand TDE it is important to realize that the thermal effect is not limited to a PSP-like pyranometer. Generally speaking, there will be "TDE" as long as the detector senses any blockages thermally in its field of view. A blockage can be a dome or a collimator and so on. An Eppley Normal Incidence Pyrheliometer (NIP) is an example: without a large thermal mass, a NIP can approach thermal equilibrium more easily than a PSP does, therefore displays a smaller "nighttime offset"; however, the sunlight or a sudden change of air temperature can cause a large thermal gradient along the cylinder of a NIP, introducing a significant thermal effect.

Figure 6a shows the output of a NIP during four rounds of tests when it is alternatively exposed and blocked from the NIST-traceable light source. Similar to a PSP, after an initial quick response to the change of light, the output of the NIP starts to drift slowly depending on temperature and its gradient in the instrument. As long as the temperature changes, the NIP's output will drift and balance to a different value. In dark conditions, the "nighttime offset" can be either positive or negative, depending on the relative temperature between the front and back

287 ends of the NIP. Note that in the fourth round when the irradiance was reduced, the temperature
288 which was measured near the window of the NIP became lower too; and it dropped several
289 degrees of Celsius further in the dark during the last few hours, as shown in Figure 6b. Notice the
290 corresponding drift of the "nighttime offset" shown in Figure 6a.

291 Figure 6c demonstrates the NIP's thermal effect in field measurements. This particular
292 example is from the 2003 ARM Aerosol IOP (Atmospheric Radiation Measurement Aerosol
293 Intensive Observation Period), when we used an ASD spectroradiometer with its appropriate
294 foreoptics [http://www.asdi.com] to measure the direct solar irradiance side-by-side with a NIP.
295 It shows that when the direct solar beam is blocked by clouds, the output of a TDE-free
296 instrument responds promptly; while the result of a TDE-laden NIP always lags behind, and can
297 drift to negative values due to the thermal effect depending on environmental conditions. Figure
298 6c also illustrates a special condition when the output of the NIP dropped below -16 W m^{-2}
299 responding to a dramatic change in temperature caused by a short passing rain shower that
300 started around 22:25 UTC on 9 May 2003 and lasted a few minutes. This example clearly
301 differentiates between surface measurements of instruments that are free of the thermal effect or
302 not.

303 This leads to why we derived a smaller f value in our previous study [*Ji and Tsay*, 2010],
304 where we explored using the combined data from a NIP and a shaded PSP as a reference to
305 demonstrate a calibration procedure. The reason is that the reference is not TDE-free; for
306 example, if TDE exists on both sides of Equation (2) and their values are identical, then the
307 derived f will erroneously become zero in a calibration. It also explains why involving a TDE-
308 laden instrument does not yield an ideal calibration reference.

309

310 **4.3. Impact on climate studies**

311 In this section we consider derivation of an aerosol's direct-radiative-effect (DRE) as an
312 example to show the potential impact of a pyranometer's thermal issues on climate studies. It is
313 based on over two months (April–June, 2008) of ground-based observations in a remote semi-
314 arid desert region frequented by dust outbreaks and local pollution during springtime in
315 northwestern China. Explicitly, with or without accounting for TDE, the measured downward
316 solar irradiance on the surface will be different which directly impacts the energy balance.
317 Implicitly, in order to simulate these different versions of measurement using a radiative transfer
318 model (RTM), some assumptions in the RTM such as the type of aerosol must be adjusted
319 accordingly. In turn, the modeling results will be altered, including DRE, throughout the column
320 of atmosphere. A brief description of the RTM and the relevant measurements are given in
321 Appendix B.

322 In this case study, a set of traditionally calibrated PSP data can be well simulated by
323 using an aerosol model of pure-dust in the RTM. However, the observed aerosols contain soot
324 emitted from local sources [*Li et al.*, 2010]. This brings a scenario that when soot is added into
325 the aerosol model while all other assumptions in the RTM remain the same, the simulated
326 downward solar irradiance on the surface will decrease, matching the TDE corrected
327 measurements. Based on ~1,700 available data points, our calculation shows that when soot
328 contributes ~1.7% of optical thickness, the irradiance decreases ~3 W m^{-2} on average. This alters
329 the aerosol's DRE from -57 to -59 W m^{-2} (-2 W m^{-2}, or +4% relative difference) on the surface;
330 from 48 to 52 W m^{-2} (4 W m^{-2}, or +8%) inside the column atmosphere; and from 9 to 7 W m^{-2} (-2

331 $W m^{-2}$, or -20%) at the top of the atmosphere. Of course, this is just one possible scenario, but it
332 demonstrates that treating TDE differently can lead to significant differences in model
333 simulations, and thus altering the interpretation of the radiative impact over the column
334 atmosphere.

335

336 **5. Conclusion and future work**

337 Using a highly stable light source in the laboratory, we have illustrated the limitation of
338 the traditional V1C1 (one-variable/measurement one-constant/calibration coefficient) calibration,
339 and demonstrated that a pyranometer can track a reference with high precision in a new V3C2
340 calibration with the thermal effect addressed. This can facilitate the quest to reduce
341 pyranometer's measurement uncertainty from over a few percent to less than 1%, which is
342 critical for climate studies. We have also highlighted some important implications of this study,
343 which included taking a pyrheliometer as an example to show that the thermal effect is not
344 limited to a pyranometer. An application of how the thermal issue can potentially impact climate
345 studies was also investigated by evaluating a direct-radiative-effect of aerosol using field
346 measurements with and without considering the pyranometer's thermal effect. Results showed
347 that model simulations of atmospheric radiative transfer are significantly altered by not
348 accounting for such effects. In short, an improved pyranometer with the thermal issue resolved
349 will have a higher precession and accuracy to help produce a more consistent dataset that can
350 play an important role in studies of climate change.

351 Although the potential of an improved pyranometer has been demonstrated under
352 controlled laboratory conditions, there are many aspects to be further explored. These include,

but are not limited to, how representative the indoor calibration at room temperature is, how the thermal expansion of a pyranometer's case and domes contributes to measurement uncertainty, and how viewing the light source sideways affects the thermal gradient in PSP. Some of these issues may be secondary, because the new calibration equation relies on stable physical properties that are less temperature-sensitive. More importantly, the cosine response is convolved with the thermal effect when the traditional calibration is used; while they can be separated in laboratory measurements once the new calibration is applied. A better understanding of the cosine response will help improve the calibration and its application to field measurements.

Additionally, it is critical to correct historical datasets for climate studies. Although a dataset can never be fully corrected without accurate TDE information, we have found that certain auxiliary measurements may be good surrogates for establishing a reasonable correction, including the temperature from a collocated pyrgeometer, or the air temperature adjacent to the pyranometer [*Ji and Tsay*, 2010]. With time, the new method can be refined to help improve solar irradiance measurements and ultimately climate studies.

Acknowledgements. This research is supported by NASA Radiation Science Program, managed by Dr. Hal B. Maring. It is also partially supported by the NASA Goddard Space Flight Center's Internal Research and Development. We thank SMARTLabs team for conducting field measurements [http://smartlabs.gsfc.nasa.gov]; CFL team for supporting laboratory calibration [http://cf.gsfc.nasa.gov]; and BORCAL team for providing outdoor calibration [http://www.nrel.gov/aim/borcal.html].

375

376 **References**

377 Ad Hoc Study Group on Carbon Dioxide and Climate (1979), Carbon Dioxide and Climate: A
378 Scientific Assessment, *National Academy of Sciences*.
379
380 Anderson, T. L., R. J. Charlson, N. Bellouin, O. Boucher, M. Chin, S. A. Christopher, J.
381 Haywood, Y. J. Kaufman, S. Kinne, J. A. Ogren, L. A. Remer, T. Takemura, D. Tanré, O.
382 Torres, C. R. Trepte, B. A. Wielicki, D. M. Winker, and H. Yu (2005), An "A-Train" strategy for
383 quantifying direct aerosol forcing of climate, *Bull. Am. Meteorol. Soc.*, doi: 10.1175/BAMS-86-
384 12-1795.
385
386 Bush, B. C., F. P. J. Valero, and A. S. Simpson (2000), Characterization of Thermal Effects in
387 Pyranometers: A Data Correction Algorithm for Improved Measurement of Surface Insolation, *J.*
388 *Atmos. Oceanic Technol.*, *17*, 165-175.
389
390 Collins, B. G. (1966), Determination of the cosine response of pyranometers, *J. Sci. Instrum.*, *43*,
391 837- 838.
392
393 Dutton, E. G., J. J. Michalsky, T. Stoffel, B. W. Forgan, J. Hickey, D. W. Nelson, T. L. Alberta,
394 and I. Reda (2001), Measurement of broadband diffuse solar irradiance using current commercial
395 instrumentation with a correction for thermal offset errors, *J. Atmos. Oceanic Technol.*, *18*, 297-
396 314, doi:10.1175/1520-0426(2001)018<0297:MOBDSI>2.0.CO;2.
397
398 Fu, Q., and K. N. Liou (1993), Parameterization of the radiative properties of cirrus clouds, *J.*
399 *Atmos. Sci.*, *50*, 2008–2025.
400
401 Fu, Q., G. Lesins, J. Higgins, and J. J. Michalsky (1999), Aerosol direct radiative forcing: a five
402 year climatology at the ARM SGP CART site, *Ninth ARM Science Team Meeting Proceedings*,
403 San Antonio, Texas, March 22-26, 1999.
404
405 Gulbrandsen, A. (1978), On the Use of Pyranometers in the Study of Spectral Solar Radiation
406 and Atmospheric Aerosols, *J. Appl. Meteor.*, *17*, 899-904.
407
408 Haeffelin, M., S. Kato, A. M. Smith, K. Rutledge, T. Charlock, and J. R. Mahan (2001),
409 Determination of the thermal offset of the Eppley Precision Spectral Pyranometer, *Appl. Opt.*,
410 *40*, 472-484.
411
412 Hansell, R. A., S.-C. Tsay, Q. Ji, N. C. Hsu, M. J. Jeong, S. H. Wang, J. S. Reid, K. N. Liou, and
413 S. C. Ou (2010), An assessment of the surface longwave direct radiative effect of airborne
414 Saharan dust during the NAMMA field campaign, *J. Atmos. Sci.*, *67*, 1408-1065, doi:
415 10.1175/2009JAS3257.1.
416
417 Haywood, J. M., P. Francis, S. Osborne, M. Glew, N. Loeb, E. Highwood, D. Tanré, G. Myhre,
418 P. Formenti, and R. Hirst (2003), Radiative properties and direct radiative effect of Saharan dust

measured by the C-130 aircraft during SHADE: 1. Solar spectrum, *J. Geophys. Res.*, *108*, D18, 8577, doi: 10.1029/2002JD002687.

IPCC Core Writing Team, Pachauri, R.K. and Reisinger, A. (Eds.) (2007), Climate change 2007: Synthesis report, Intergovernmental Panel on Climate Change, Geneva, Switzerland. pp 104. (Available at http://www.ipcc.ch/pdf/assessment-report/ar4/syr/ar4_syr.pdf)

ISO 9846 (1993), Solar energy – Calibration of a pyranometer using a pyrheliometer.

Ji, Q. and S.-C. Tsay (2000), On the dome effect of Eppley pyrgeometers and pyranometers, *Geophys. Res. Lett.*, *27*, 971-974.

Ji, Q. and S.-C. Tsay (2010), A novel non-intrusive method to resolve the thermal-dome-effect of pyranometers: Instrumentation and observational basis, *J. Geophys. Res.*, *115*, D00K21, doi:10.1029/2009JD013483.

Li, C., S.-C. Tsay, J. S. Fu, R. R. Dickerson, Q. Ji, S. W. Bell, Y. Gao, W. Zhang, J. Huang, Z. Li, and H. Chen (2010), Anthropogenic air pollution observed near dust source regions in northwestern China during springtime 2008, *J. Geophys. Res.*, *115*, D00K22, doi:10.1029/2009JD013659.

Liou, K., Q. Fu, and T. Ackerman (1988), A simple formulation of the delta-four-stream approximation for radiative transfer parameterizations, *J. Atmos. Sci.*, *45*, 1940–1947.

McComiskey, A., S. E. Schwartz, B. Schmid, H. Guan, E. R. Lewis, P. Ricchiazzi, and J. A. Ogren (2008), Direct aerosol forcing: Calculation from observables and sensitivities to inputs, *J. Geophys. Res.*, 113, D09202, doi:10.1029/2007JD009170.

Michalsky, J. J., L. C. Lee, W. E. Berkheiser, III (1995), Cosine response characteristics of some radiometric and photometric sensors, *Solar Energy*, *54*, No. 6, 397-402.

Michalsky J. J., R. Dolce, E. G. Dutton, M. Haeffelin, G. Major, J. A. Schlemmer, D. W. Slater, J. R. Hickey, W. Q. Jeffries, A. Los, D. Mathias, L. J. B. McArthur, R. Philipona, I. Reda, and T. Stoffel (2003), Results from the first ARM diffuse horizontal shortwave irradiance comparison *J. Geophys. Res.*, *108*, D3, 4108, doi:10.1029/2002JD002825.

Trenberth, J. E., J. T. Fasullo, and J. Kiehl (2009), Earth's global energy budget, *Bull. Am. Meteorol. Soc.*, 90, 311–323, doi:10.1175/2008BAMS2634.1.

Walker, J., C. L. Cromer, and J. T. McLean (1991), A technique for improving the calibration of large-area sphere sources, *Proc. SPIE*, *1493*, 224-230.

Wild, M. (2009), Global dimming and brightening: A review, *J. Geophys. Res.*, *114*, D00D16, doi:10.1029/2008JD011470.

464 WMO (2008), Guide to Meteorological Instruments and Methods of Observation (7th edition),
465 *WMO-No.8*, World Meteorological Organization, Geneva.
466

Appendix A. Two methods for measuring a pyranometer's effective dome temperature (i.e., T_d)

While its case temperature, T_c, can be captured directly by putting a thermistor inside a pyranometer, its effective dome temperature, T_d, cannot be as easily measured. In a method illustrated in Figure A1, the space between a PSP's domes can be converted into a constant-volume gas thermometer [*Ji and Tsay*, 2010]; therefore, T_d is derived from a pressure measurement by applying the ideal gas law. Figure A1 also depicts an alternative method that still relies on a pressure measurement and the ideal gas law, but does not require any modification to the instrument other than adding a thermistor and attaching a barometer to the case of a pyranometer. Here we summarize how these methods work.

(a) For a sealed volume, the ideal gas law states that,

$$T_d = P_d / r, \tag{A1}$$

where P_d is the pressure measured by a barometer, and r is a constant proportional to the density of the trapped air between the domes. r can be determined under dark conditions when the thermal gradient diminished (i.e., where V=0 and T_d=T_c thus r=P_d/T_d=P_d/T_c).

(b) The attached barometer is for capturing the air pressure, P, inside the whole instrument. For simplification, we assume that T_d and T_c represent the temperatures above and beneath the receiving surface of thermopile, respectively. According to the ideal gas law, when the pyranometer reaches thermal equilibrium at a given temperature T_0 (i.e., T_d=T_c=T_0), the pressure inside the instrument will be:

$$P_0 = \frac{m_d + m_c}{v_d + v_c} T_0, \tag{A2}$$

488 where m_d and m_c are proportional respectively to the masses of air occupying the volume above
489 the thermopile (i.e., v_d), and elsewhere inside the case (i.e., v_c). Normally $T_d \neq T_c$ and $P \neq P_0$
490 without thermal equilibrium; however, P is always the same in both v_d and v_c, therefore
491 simultaneously,

492 $$P = \frac{m_d}{v_d} T_d, \text{ and } P = \frac{m_c}{v_c} T_c. \quad \text{(A3)}$$

493 Let $q = v_d/(v_c+v_d)$ and using Equations (A2) and (A3), we have:

494 $$T_d = \frac{q}{(P_0/T_0)/(P/T_c) - (1-q)} T_c. \quad \text{(A4)}$$

495 Here P_0/T_0 is proportional to the density of the trapped air inside a pyranometer, and ideally
496 remains a constant if there is no thermal expansion of the instrument or leak of air. In addition, q
497 defines the fraction of the volume above the thermopile over the total volume inside the
498 instrument. We found that the volume between the domes consists of ~13% of the total volume
499 inside a PSP. After compensating for the part between the inner dome and thermopile, we
500 derived $q \approx 0.23$. Although q is well defined in geometry, its effective value may vary slightly
501 depending on thermal expansion or other factors, such as which part of air is effectively
502 contributing to T_d. Nevertheless, once P_0/T_0 and q are measured, T_d is determined from T_c and P.

503

504 **Appendix B. Radiative transfer model (RTM) and relevant measurements**

505 A publicly available multiple-scattering plane-parallel RTM has been used for estimating
506 the shortwave (SW) irradiances near the ground surface and at the top of the atmosphere (TOA).

507 The model was developed by Fu-Liou [*Liou et al.*, 1988; *Fu and Liou*, 1993] and later modified
508 and distributed by the NASA Langley group [http://snowdog.larc.nasa.gov/rose/fu0602].
509 Originally the SW spectrum in this RTM is divided into 6 bands (0.2–0.7, 0.7–1.3, 1.3–1.9, 1.9–
510 2.5, 2.5–3.5, and 3.5–4.0 μm; with the first band further divided into 10 sub-bands). In order to
511 be consistent with the measurements, we weight the calculated irradiances in those bands
512 according to the transmittance values for the pyranometer glass dome. The longwave irradiance
513 is also calculated in the model [see *Hansell et al.*, 2010], although the signal to noise ratio is
514 much smaller from aerosol such as dust. The major input parameters for the RTM are listed in
515 Table B1, while the minor ones such as trace gases remain at the model's default values.

516 The relevant measurements that are used for constraining the RTM are, (1) a Cimel
517 sunphotometer [http://aeronet.gsfc.nasa.gov] for aerosol optical depth (AOD) at 0.34, 0.38, 0.44,
518 0.5, 0.67, 0.87, and 1.02 μm, and column precipitable water vapor (PWV); (2) a micro-pulse
519 lidar [MPL, http://mplnet.gsfc.nasa.gov] for backscatter profile; (3) sounders
520 [http://weather.uwyo.edu/upperair/sounding.html] for temperature and relative humidity (average
521 from two closest sites at Jiuquang and Minqin in China); (4) a UV radiometer for column ozone;
522 (5) a ASD spectroradiometer for surface spectral albedo; and (6) PSP pyranometers for
523 downward SW irradiance on the surface. The measurement site is located in a semiarid desert
524 area on a dry riverbed sparsely coved by tumbleweed.

525 A mid-latitude summer atmosphere profile included in the model is regarded as a
526 template and updated with the available sounding data. Subsequently the updated profiles are
527 scaled to match the measured column ozone and PWV amounts. The instantaneous AOD at the
528 seven Cimel wavelengths are distributed proportionally to the normalized relative backscatter
529 observed by the MPL. The model simulation is performed only when a cloud screened Cimel

530 observation is available. All the inputs to the model are linearly interpolated to the time stamp of
531 the Cimel measurements.

532 Aerosol's shortwave direct-radiative-effect (DRE) is defined as a perturbation in net-
533 irradiance given by the difference between the incoming and outgoing radiative energies caused
534 by aerosols when compared to an aerosol-free reference. In other words, regarding the incoming
535 irradiance (I) is as positive from the perspective of each location, DRE=$\delta I(\tau)$-$\delta I(0)$; where, at
536 TOA $\delta I_{TOA}=I_{TOA}^{\uparrow}-I_{TOA}^{\downarrow}$, across the column atmosphere $\delta I_{atm}=I_{TOA}^{\downarrow}+I_{surface}^{\uparrow}-I_{TOA}^{\uparrow}-I_{surface}^{\downarrow}$, and on
537 the surface $\delta I_{surface}=I_{surface}^{\downarrow}-I_{surface}^{\uparrow}$. Except for an imaginary aerosol-free condition (τ=0), $\delta I(0)$ is
538 a modeled state with the same atmospheric properties as for $\delta I(\tau)$. Notice that since $\delta I(0)$ does
539 not exist in reality, therefore DRE is not a directly measureable parameter. Our calculated DRE
540 are instantaneous values [e.g., *Haywood et al.*, 2003] based on the time stamp of the Cimel
541 sunphotometer, versus diurnally averaged quantities [e.g., *Anderson et al.*, 2005].

542 Uncertainties in broadband irradiance measurements can contribute to inaccurate
543 assessments of aerosol's DRE. For example, SW pyranometers can introduce measurement errors
544 due to the instrument's cosine response [e.g., *Collins*, 1966; *Michalsky et al.*, 1995]. In a study of
545 DRE, *Fu et al.* [1999] concluded that discrepancies between modeled and measured irradiance
546 can be largely due to the radiation measurement errors. Other studies [e.g., *McComisky et al.*
547 2008] have also examined the sensitivity of DRE to various model parameters (i.e., aerosol and
548 surface properties, etc); however, the impact of TDE to the determination of DRE has not caught
549 much attention.

550

551 **Figure A1.** Schematically, a PSP is a thermopile mounted on a metal case and covered by two
552 layers of glass dome. The interior of PSP is isolated from the environment. The thermopile
553 outputs a voltage V. (a) By sealing the space between the two domes and adding measurements
554 of T_c and P_d, we can determine the effective dome temperature, T_d, via Equation (A1). In
555 addition, the temperature of the receiving surface of thermopile, T_s, is a function of V and T_c. (b)
556 Without sealing the space between the two domes, T_d can still be determined from T_c and the
557 pressure of the trapped air inside the whole PSP, P, using Equation (A4).
558
559 **Figure 1.** (a) Grande is a 1-meter Teflon integrating sphere with an aperture of 25.40 cm in
560 diameter. It has 9 independently-controlled lamps for producing different levels of radiance. A
561 PSP can be mounted with the thermopile facing the aperture. (b) The irradiance from Grande is
562 determined by a combination of its spectral radiance, viewing geometry, and spectral cut-off of
563 PSP's dome. The gray curve illustrates a transmittance for WG295 glass. The bold curve
564 highlights the currently NIST-traceable part of spectral radiance (i.e., between 0.4 and 2.4 μm).
565
566 **Figure 2.** Example of eight rounds of calibration which took about three hours. (a) The light is
567 turned on at point A, making all the measured temperatures in a PSP to increase (see Section 3).
568 The light is blocked at point B about fifteen minutes later, causing the temperatures to decrease
569 and approach each other. The thermal equilibrium is reached after several minutes. The light is
570 turned on again at point C, followed by a reduction of the light intensity at point D. The similar
571 pattern is repeated in the later rounds. (b) The pressure in the sealed volume between domes (c.f.,
572 Appendix A). (c) The varying output voltage of thermopile. See section 3 for details.
573

574 **Figure 3.** The *I/V* is the calibration factor that should be a constant according to the traditional
575 calibration equation. For example, it should remain at 133.95 W m^{-2} mV^{-1} according to a
576 BORCAL result, marked by the solid line. In reality *I/V* varies with temperature across a wide
577 range as shown in the bold curve. See section 3.1 for details.
578
579 **Figure 4.** Example of the new calibration. (a) A consistent result from selected rounds. (b)
580 Including additional rounds. (c) Same as above, but without modification to the PSP (c.f.,
581 Appendix A). See section 3.2 for details.
582
583 **Figure 5.** The traditional (bold curve) versus the new (thin curve) calibration results. The
584 sampling rate is about every 5 seconds. The PSP is exposed to light at point A, then blocked
585 from light at point B, and exposed to light again at point C. The arrows highlight that the new
586 calibration tracks the correct irradiance promptly. (a) Notice that the traditional result is slightly
587 different in period C to D from in period A to B. (b) The prolonged non-zero results of the
588 traditional calibration in dark conditions. See section 3.3 for details.
589
590 **Figure 6.** Thermal behavior of NIP. (a) In round 1 the light was turned on at point A; and after
591 rose from 0 to ~0.074 mV swiftly, the output voltage of the NIP, V_{NIP}, drifted slowly up to ~0.13
592 mV in about half an hour. At point B the light is blocked; and V_{NIP} dropped halfway to ~0.06
593 mV quickly, then started to drift toward 0 mV slowly. This was repeated three more rounds with
594 V_{NIP} reached slightly different values depending on the environmental temperature. In round 4
595 the light intensity was set to 75% of that in the previous rounds. (b) The temperature, T,
596 increased when the light was on, and decreased when the light was blocked. (c) An example

showing about an hour and half of data in the late afternoon on 9 May 2003. The solid curve is for a TDE-free ASD spectroradiometer, and the dotted curve is for a NIP. There was a rain shower during the shaded period. See section 4.2 for details.

Table 1. Sample calibration results of a PSP using different types of domes

Type of dome	f	c (W m^{-2} mV^{-1})
WG295 #1	1.5	130
WG295 #2 [a]	1.5	130
GG395 (yellow dome) [a]	1.5	124
RG695 (red dome) [a]	1.8	128
WG295 #3 [b]	1.5	130
Quartz [c]	1.3	129
WG295 #4 [d]	1.6	132
WG295 #4 [e]	1.7	133
WG295 #5 [f]	2.0	130.3
WG295 #5 [g]	1.9	130

[a] same inner dome as in WG295 #1
[b] a different set of inner and outer domes
[c] the transmittance is assumed to be 100% between 0.2 and 3.5 μm, 0% elsewhere
[d] yet another set of inner and outer domes; mounted on a brass collar for testing
[e] same as above, except sealed
[f] one more set of sealed inner and outer domes
[g] same as above, except unsealed

610 **Table B1.** Major inputs for the radiative transfer model

Parameter	Source	Comment
Location	Observation	Zhangye Climatological Observatory (~1.5 km above sea level, 100°16.575'E, 39°4.940'N).
Atmospheric profile	Observation and model	Modeled "mid-latitude summer" profile if sounding and other measurements are lacking.
Solar incident angle	Observation	Determined by location and time.
Surface albedo	Observation	Interpolated to the model bands of wavelength.
Aerosol optical depth	Observation	At 7 sun-photometer wavelengths.
Water vapor	Observation and model	Combination of sounding and modeled profile; scaled to match sun-photometer measurement.
Aerosol type	Model	Defined in model. The one most consistent with observations is selected.
Aerosol distribution	Observation and model	Based on the modeled profile; updated according to the MPL backscatter.
Cloud type	Model	Only the cloud-screened conditions are simulated.

611

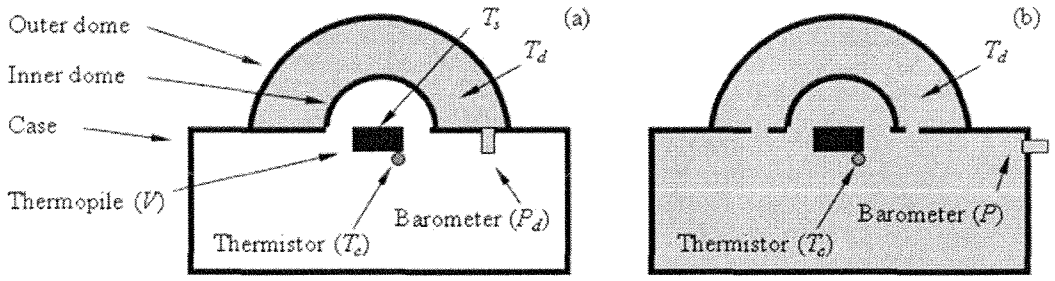

612

613 **Figure A1.** Schematically, a PSP is a thermopile mounted on a metal case and covered by two
614 layers of glass dome. The interior of PSP is isolated from the environment. The thermopile
615 outputs a voltage V. (a) By sealing the space between the two domes and adding measurements
616 of T_c and P_d, we can determine the effective dome temperature, T_d, via Equation (A1). In
617 addition, the temperature of the receiving surface of thermopile, T_s, is a function of V and T_c. (b)
618 Without sealing the space between the two domes, T_d can still be determined from T_c and the
619 pressure of the trapped air inside the whole PSP, P, using Equation (A4).

620

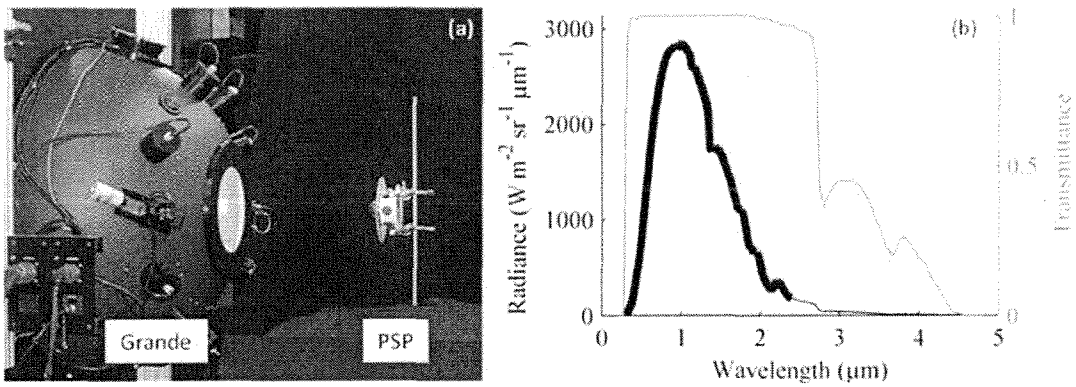

621

622 **Figure 1.** (a) Grande is a 1-meter Teflon integrating sphere with an aperture of 25.40 cm in
623 diameter. It has 9 independently-controlled lamps for producing different levels of radiance. A
624 PSP can be mounted with the thermopile facing the aperture. (b) The irradiance from Grande is
625 determined by a combination of its spectral radiance, viewing geometry, and spectral cut-off of
626 PSP's dome. The gray curve illustrates a transmittance for WG295 glass. The bold curve
627 highlights the currently NIST-traceable part of spectral radiance (i.e., between 0.4 and 2.4 µm).

628

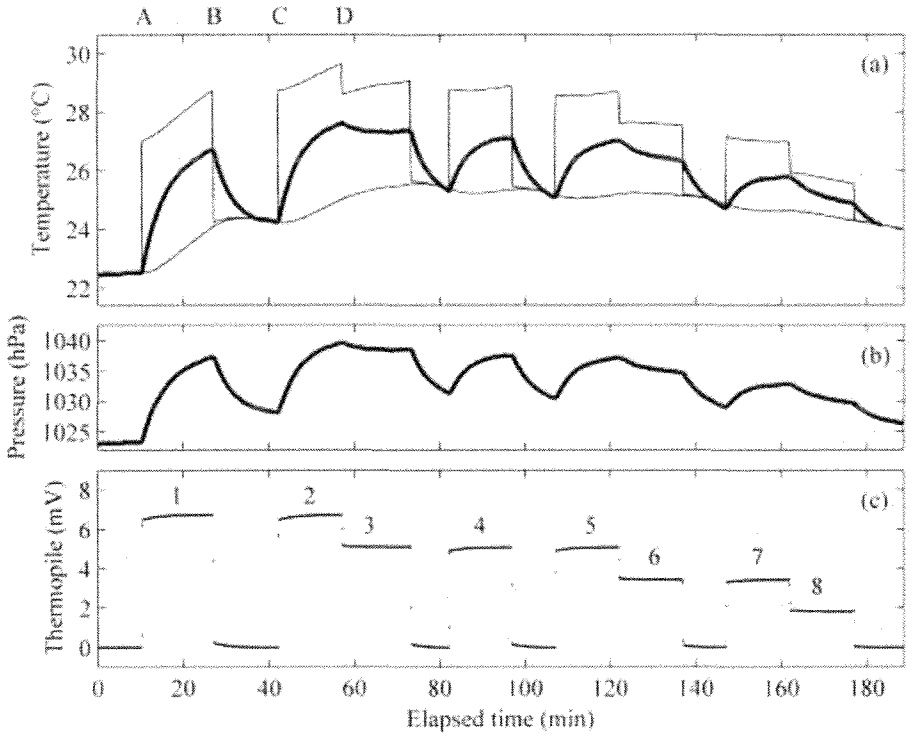

629

630 **Figure 2.** Example of eight rounds of calibration which took about three hours. (a) The light is
631 turned on at point A, making all the measured temperatures in a PSP to increase (see Section 3).
632 The light is blocked at point B about fifteen minutes later, causing the temperatures to decrease
633 and approach each other. The thermal equilibrium is reached after several minutes. The light is
634 turned on again at point C, followed by a reduction of the light intensity at point D. The similar
635 pattern is repeated in the later rounds. (b) The pressure in the sealed volume between domes (c.f.,
636 Appendix A). (c) The varying output voltage of thermopile. See section 3 for details.

637

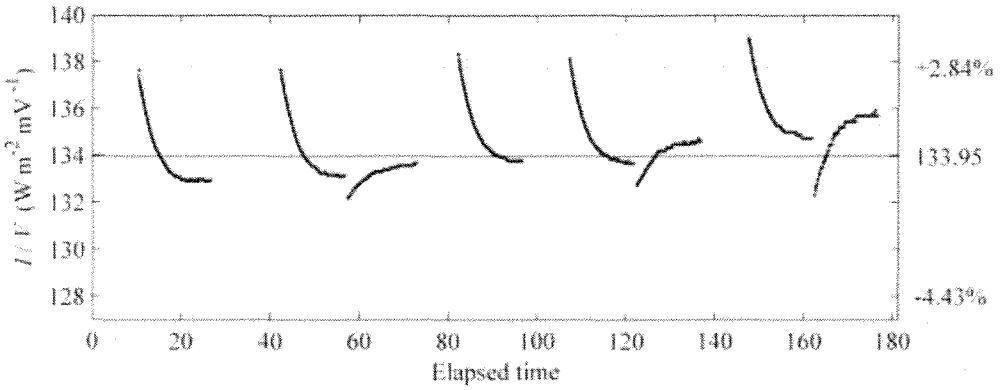

638

639 **Figure 3.** The *I/V* is the calibration factor that should be a constant according to the traditional
640 calibration equation. For example, it should remain at 133.95 W m^{-2} mV^{-1} according to a
641 BORCAL result, marked by the solid line. In reality *I/V* varies with temperature across a wide
642 range as shown in the bold curve. See section 3.1 for details.

643

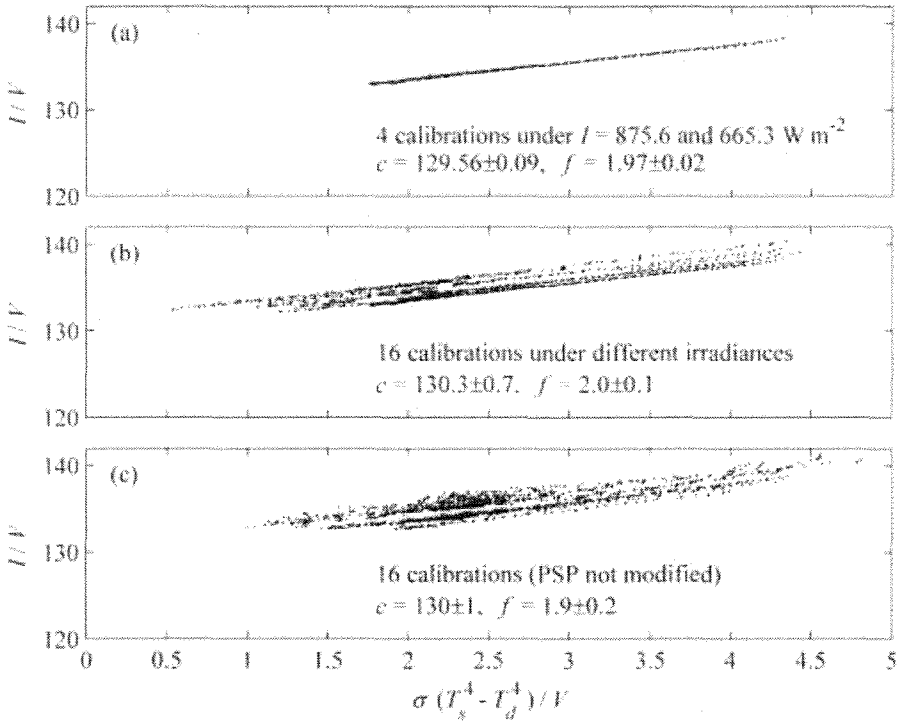

644

645 **Figure 4.** Example of the new calibration. (a) A consistent result from selected rounds. (b)
646 Including additional rounds. (c) Same as above, but without modification to the PSP (c.f.,
647 Appendix A). See section 3.2 for details.

648

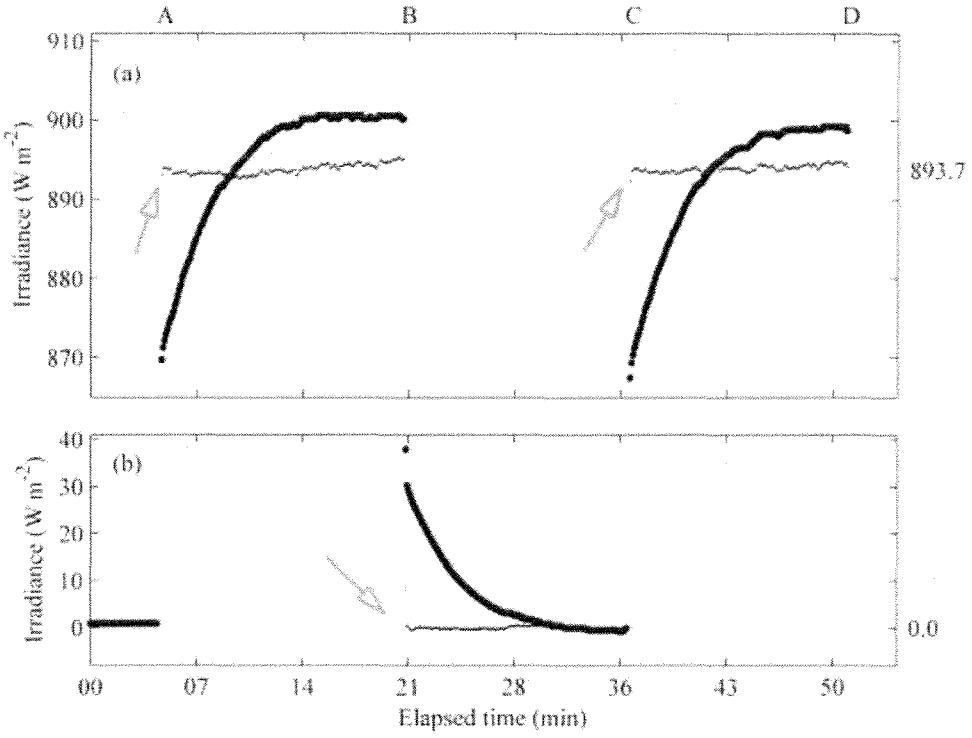

649

650 **Figure 5.** The traditional (bold curve) versus the new (thin curve) calibration results. The
651 sampling rate is about every 5 seconds. The PSP is exposed to light at point A, then blocked
652 from light at point B, and exposed to light again at point C. The arrows highlight that the new
653 calibration tracks the correct irradiance promptly. (a) Notice that the traditional result is slightly
654 different in period C to D from in period A to B. (b) The prolonged non-zero results of the
655 traditional calibration in dark conditions. See section 3.3 for details.

656

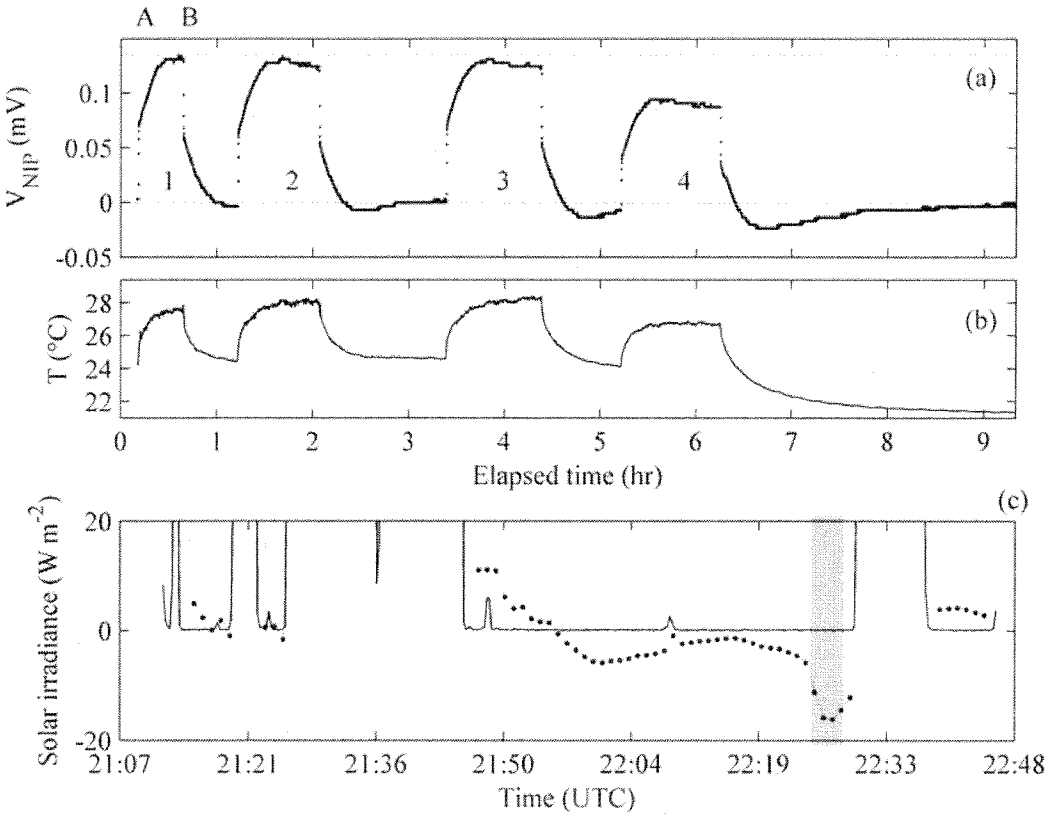

657

658 **Figure 6.** Thermal behavior of NIP. (a) In round 1 the light was turned on at point A; and after
659 rose from 0 to ~0.074 mV swiftly, the output voltage of the NIP, V_{NIP}, drifted slowly up to ~0.13
660 mV in about half an hour. At point B the light is blocked; and V_{NIP} dropped halfway to ~0.06
661 mV quickly, then started to drift toward 0 mV slowly. This was repeated three more rounds with
662 V_{NIP} reached slightly different values depending on the environmental temperature. In round 4
663 the light intensity was set to 75% of that in the previous rounds. (b) The temperature, T,
664 increased when the light was on, and decreased when the light was blocked. (c) An example
665 showing about an hour and half of data in the late afternoon on 9 May 2003. The solid curve is
666 for a TDE-free ASD spectroradiometer, and the dotted curve is for a NIP. There was a rain
667 shower during the shaded period. See section 4.2 for details.